

1 Studies of uniformity of 50  $\mu\text{m}$  low-gain avalanche detectors  
2 at the Fermilab test beam.

3 A. Apresyan<sup>\*,a</sup>, S. Xie<sup>b</sup>, C. Pena<sup>b</sup>, R. Arcidiacono<sup>e,g</sup>, N. Cartiglia<sup>e</sup>, M. Carulla<sup>h</sup>,  
4 G. Derylo<sup>a</sup>, M. Ferrero<sup>e</sup>, D. Flores<sup>h</sup>, P. Freeman<sup>d</sup>, Z. Galloway<sup>d</sup>, A. Ghassemi<sup>i</sup>, H. Al  
5 Ghoul<sup>c</sup>, L. Gray<sup>a</sup>, S. Hidalgo<sup>h</sup>, S. Kamada<sup>i</sup>, S. Los<sup>a</sup>, M. Mandurrino<sup>e</sup>, A. Merlos<sup>h</sup>,  
6 N. Minafra<sup>c</sup>, A. Ronzhin<sup>a</sup>, G. Pellegrini<sup>h</sup>, D. Quirion<sup>h</sup>, C. Royon<sup>c</sup>, H. Sadrozinski<sup>d</sup>,  
7 A. Seiden<sup>d</sup>, V. Sola<sup>e</sup>, M. Spiropulu<sup>b</sup>, A. Staiano<sup>e</sup>, L. Uplegger<sup>a</sup>, K. Yamamoto<sup>i</sup>,  
8 K. Yamamura<sup>i</sup>

9 <sup>a</sup>*Fermi National Accelerator Laboratory, Batavia, IL, USA*

10 <sup>b</sup>*California Institute of Technology, Pasadena, CA, USA*

11 <sup>c</sup>*University of Kansas, KS, USA*

12 <sup>d</sup>*SCIPP, University of California Santa Cruz, CA, USA*

13 <sup>e</sup>*INFN, Torino, Italy*

14 <sup>f</sup>*Università di Torino, Torino, Italy*

15 <sup>g</sup>*Università del Piemonte Orientale, Italy*

16 <sup>h</sup>*Centro Nacional de Microelectrónica (IMB-CNM-CSIC), Barcelona, Spain*

17 <sup>i</sup>*Hamamatsu Photonics (HPK), Hamamatsu, Japan*

---

18 **Abstract**

In this paper we report measurements of the uniformity of time resolution, signal amplitude, and charged particle detection efficiency across the sensor surface of low-gain avalanche detectors (LGAD). Comparisons of the performance of sensors with different doping concentrations and different active thicknesses are presented, as well as their temperature dependance and radiation tolerance up to  $6 \times 10^{14} \text{ n/cm}^2$ . Results were obtained at the Fermilab test beam facility using 120 GeV proton beams, and a high precision pixel tracking detector. LGAD sensors manufactured by the Centro Nacional de Microelectrónica (CNM) and Hamamatsu Photonics (HPK) were studied. The uniformity of the sensor response in pulse height before irradiation was found to have a 2% spread. The signal detection efficiency and timing resolution in the sensitive areas before irradiation were found to be 100% and 30-40 ps, respectively. A “no-response” area between pads was measured to be about 130  $\mu\text{m}$  for CNM and 170  $\mu\text{m}$  for HPK sensors. After a neutron fluence of  $6 \times 10^{14} \text{ n/cm}^2$  the CNM sensor exhibits a large gain variation of up to a factor of 2.5 when comparing metalized and non-metalized sensor areas. An irradiated CNM sensor achieved a time resolution of 30 ps for the metalized area and 40 ps for the non-metalized area, while a HPK sensor irradiated to the same fluence achieved a 30 ps time resolution.

19 **Key words:**

20 Silicon, Timing, LGAD, Test Beam

---

<sup>21</sup>	<b>Contents</b>	
<sup>22</sup>	<b>1 Introduction</b>	<b>2</b>
<sup>23</sup>	<b>2 Experimental Setup</b>	<b>3</b>
<sup>24</sup>	<b>3 LGAD Sensor Properties</b>	<b>4</b>
<sup>25</sup>	<b>4 Readout Electronics</b>	<b>6</b>
<sup>26</sup>	<b>5 Timestamp Reconstruction</b>	<b>7</b>
<sup>27</sup>	<b>6 Sensor Studies and Analysis</b>	<b>8</b>
<sup>28</sup>	6.1 Study of the uniformity of the LGAD sensors . . . . .	9
<sup>29</sup>	6.2 Measurement of the “no-response” area between two neighboring pixels . .	11
<sup>30</sup>	6.3 Comparison of HPK doping profiles . . . . .	12
<sup>31</sup>	6.4 Comparison of uniformity of HPK 50 $\mu\text{m}$ with 80 $\mu\text{m}$ . . . . .	14
<sup>32</sup>	6.5 Temperature dependence of the LGAD sensors . . . . .	14
<sup>33</sup>	6.6 Radiation tolerance of the LGADs . . . . .	19
<sup>34</sup>	<b>7 Conclusion</b>	<b>27</b>

### <sup>35</sup> 1. Introduction

<sup>36</sup> Future colliders, including the high luminosity upgrade of the Large Hadron Collider  
<sup>37</sup> (HL-LHC) at CERN, will operate with an order of magnitude higher instantaneous lu-  
<sup>38</sup> minosity compared to what has been achieved at the large hadron collider (LHC) so  
<sup>39</sup> far. With the increased instantaneous luminosity, the rate of simultaneous interactions  
<sup>40</sup> per bunch crossing (pileup) is projected to reach an average of 140 to 200. The large  
<sup>41</sup> amount of pileup increases the difficulties in separating particles from the hard scatter-  
<sup>42</sup> ing interaction with those produced in different pileup interactions. In particular, the  
<sup>43</sup> ability to discriminate between jets produced in the events of interests, especially those  
<sup>44</sup> associated with vector boson fusion processes, and jets produced by pileup interactions  
<sup>45</sup> will be degraded. Additionally, the efficiency to identify high  $p_{\text{T}}$  isolated electrons and  
<sup>46</sup> muons will be severely reduced due to the high density of pileup particles in their vicinity.  
<sup>47</sup> The missing transverse energy resolution will also deteriorate, and several other physics  
<sup>48</sup> objects performance metrics will also suffer the detrimental effects of pileup.

<sup>49</sup> One way to mitigate the pileup effects mentioned above, complementary to precision  
<sup>50</sup> tracking methods, is to perform a time of arrival measurement associated with each par-  
<sup>51</sup> ticle. Such a measurement with a precision of about 30-40 ps, will reduce the effective  
<sup>52</sup> amount of pileup by a factor of 10, given that the spread in collision time of the pileup  
<sup>53</sup> interactions at HL-LHC is foreseen to be approximately 200 ps. It has been previously  
<sup>54</sup> shown that a precision of better than 20 ps can be achieved for electromagnetic showers  
<sup>55</sup> measured with silicon sampling calorimeters [? ? ?] using traditional planar silicon

---

\*Corresponding author  
*Email address:* apresyan@fnal.gov (A. Apresyan)

detectors. In this paper, we report results of particle beam measurements with thin low-gain avalanche detectors (LGAD) that have been shown to achieve time resolutions around 30 ps [? ? ]. LGAD are envisioned to be used in the CMS and ATLAS experiment upgrades for HL-LHC in order to overcome the event reconstruction challenges posed by the high rate of concurrent collisions per beam crossing. The implemented regions of pseudorapidity ( $\eta$ ) are:  $|\eta| > 1.5$ , and  $2.4 < |\eta| < 4.2$  for CMS and ATLAS, respectively. In order to achieve the desired timing precision across a large area of the detectors, the sensors will need to provide high uniformity of signal response and timing resolution. In this paper, we perform detailed measurements of the performance of LGAD sensors produced by Centro Nacional de Microelectrónica (CNM) and Hamamatsu Photonics (HPK) exposed to the 120 GeV proton beam at Fermilab. Utilizing high-precision tracking detectors we extract position dependence of the charged-particle detection efficiency, signal pulse height, signal timestamp, and time resolution of 50  $\mu\text{m}$  LGAD sensors. We also compare the uniformity of 50 and 80  $\mu\text{m}$  LGAD sensors. Uniformity and time resolution of the HPK and CNM sensors irradiated to an equivalent neutron fluence of  $6 \times 10^{14} \text{ n/cm}^2$  are also presented. Detailed measurements of irradiated HPK sensors were presented in Ref. [? ].

The paper is organized as follows: the experimental setup is described in Sec. 2; the tested LGAD sensors and their operating conditions are listed in Sec. 3; readout electronics used in the measurements are described in Sec. 4; algorithms used in the event reconstruction are described in Sec. 5; beam test results are presented in Sec. 6, followed by the conclusion in Sec. 7.

## 2. Experimental Setup

Test-beam measurements were performed at the Fermilab Test-beam Facility (FTBF) which provided a 120 GeV proton beam from the Fermilab Main Injector accelerator. The Devices Under Test (DUTs) were mounted on a remotely operated motorized stage, placed inside the pixel telescope detector [? ]. The latter provides better than 10  $\mu\text{m}$  position resolution for charged particles impinging on the DUT. Additionally, a Photek 240 micro-channel plate (MCP-PMT) detector [? ? ? ? ] was placed furthest downstream, and provided a very precise reference timestamp. Its precision has been previously measured to be less than 7 ps [? ]. A schematic diagram and photograph of the experimental area are shown in Fig. 1 and Fig. 2, respectively.

The DAQ system for the DUTs and the Photek MCP-PMT is based on a CAEN V1742 digitizer board [? ], which provides digitized waveforms sampled at 5 GS/s, and with one ADC count corresponding to 0.25 mV. The CAEN digitizer was voltage- and time-calibrated using the procedure described in Ref. [? ]. One of the main parameters of DAQ system for precise time measurements is the “electronic time resolution”, defined as the measured time jitter between two signals that are split from the same source. These two signals are used as “start” and “stop” signals to electronic system measuring the time interval between them. The electronic time resolution of the CAEN V1742 digitizer was measured to be less than 4 ps, and thus, its impact on the timing measurements presented in these studies can be neglected. The DAQ for the pixel telescope is based on the CAPTAN system developed at Fermilab [? ]. The track-reconstruction is performed using the Monicelli software package developed specifically for the test-beam application.

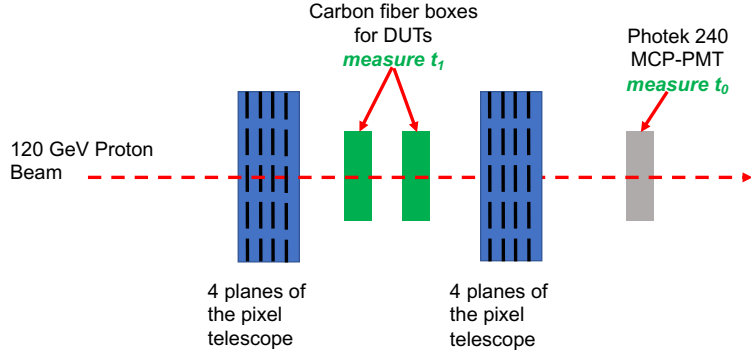


Figure 1: A schematic diagram of the test-beam setup is shown. The  $t_0$  and  $t_1$  are defined in Section 4.

100        The DUTs were placed inside the telescope box described in Ref.[? ], and mounted on  
 101      an aluminum mechanical support structure. The telescope box can be moved remotely  
 102      in both the horizontal and vertical directions in order to align the DUTs with the beam.  
 103      The aluminum support structure for the DUTs provide both mechanical stability and  
 104      are equipped with Peltier cooling elements that were used in this study to operate the  
 105      DUTs at  $-10^\circ$  and  $-20^\circ$  C.

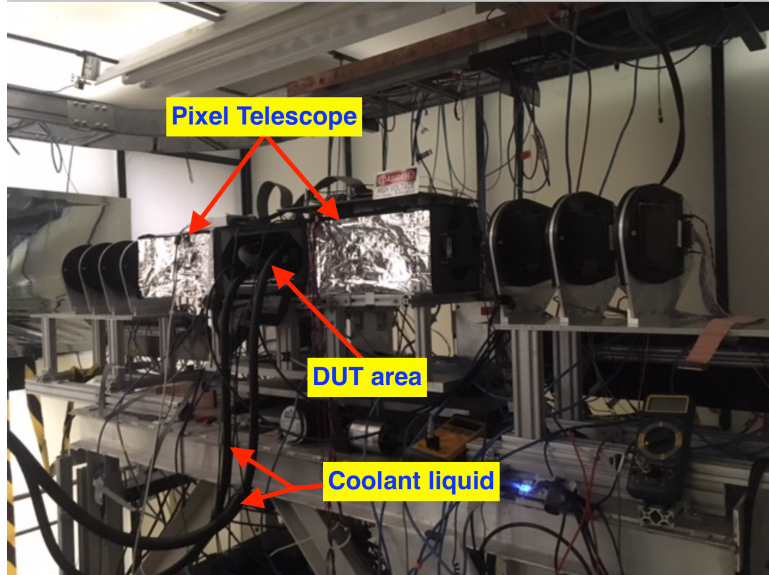


Figure 2: A picture of the experimental area. Thea pixel telescope detectors are placed inside the electrostatic-discharge shielded boxes on the two sides of the DUT area. Cooling liquid for the Peltier elements inside the DUT area is provided by the two tubes shown in the picture.

106        The beam is resonantly extracted in a slow spill for each Main Injector cycle delivering  
 107      a single 4.2 sec long spill per minute. The primary beam (bunched at 53 MHz) consists

108 of 120 GeV protons. All measurements presented in this paper were taken with the  
 109 primary beam particles. The trigger to both the CAEN V1742 and to the pixel telescope  
 110 was provided by a scintillator mounted on a photomultiplier tube, placed upstream of  
 111 the DUTs in the beam-line. Due to the limited buffer depth of the CAEN V1742 board,  
 112 special care had to be taken in the design of the DAQ system to ensure that both the DUT  
 113 and telescope DAQs collect exactly the same amount of triggers. This was achieved by  
 114 limiting the trigger rate by introducing an adjustable dead-time using a custom-designed  
 115 trigger board. Processed data from the pixel telescope and the DUTs were merged offline  
 116 by matching the trigger counters recorded by the two systems.

### 117 3. LGAD Sensor Properties

118 Sensors manufactured by HPK and CNM were measured in the test beam experiment.  
 119 Both single- and four-channel configurations of the sensor were used in the measurements.  
 120 The sensors studied have active thicknesses of about 50  $\mu\text{m}$  and 80  $\mu\text{m}$ . A brief summary  
 121 of the sensors dimensions and capacitances is presented in Tab. 1.

122 CNM sensors have an active thickness of about 45  $\mu\text{m}$  and were produced on 4-inch  
 123 Silicon-on-Insulator wafers with a 45  $\mu\text{m}$  thick high resistivity float zone (FZ) active layer  
 124 on top of a 1  $\mu\text{m}$  buried oxide and a 300  $\mu\text{m}$  support wafer. The back-side contact is  
 125 achieved through wet-etched deep access holes through the insulator. The dose of the  
 126 boron implantation for the W9HG11 sensor is  $1.9 \times 10^{13}$  atoms/cm $^{-2}$ , and  $2.0 \times 10^{13}$   
 127 atoms/cm $^{-2}$  for the W11LGA35. Details on CNM sensors can be found in Ref. [? ?].

128 The HPK sensors were manufactured on 6-inch silicon wafers of 150  $\mu\text{m}$  total thickness  
 129 with a 50  $\mu\text{m}$  or 80  $\mu\text{m}$  thick high resistivity float zone (FZ) active layer. Four gain splits,  
 130 identified with the letters A (lowest gain) to D (highest gain), were produced identical  
 131 in the mask design but with a different  $p^+$  dose of the gain layer to study the optimal  
 132 parameters for fast timing detectors. The pads were produced in three versions: two with  
 133 guard ring (GR and GBGR) and one without guard ring. Four-channel sensors in a  $2 \times 2$   
 134 array were produced with all 4 gain-splits, and are identified with the PIX identifier. For  
 135 example, the  $2 \times 2$  array of the 50  $\mu\text{m}$  sensor split D is labeled as 50D-PIX. The sensor  
 136 corresponding to each of the four channels in the array is also referred to as a pixel in  
 137 this paper. Each pixel in the  $2 \times 2$  HPK array has dimensions of  $3 \times 3 \text{ mm}^2$ . The CNM  
 138 single-channel sensors are square pads with an active area of  $1.7 \text{ mm}^2$  while the HPK  
 139 single-channel sensors are circular pads with an active area of  $0.8 \text{ mm}^2$ .

Sensor	Number of channels	Single channel dimensions	Single channel capacitance
HPK 50A-PIX	4	$3 \times 3 \text{ mm}^2$	20 pF
HPK 50B-PIX	4	$3 \times 3 \text{ mm}^2$	20 pF
HPK 50C-PIX	4	$3 \times 3 \text{ mm}^2$	20 pF
HPK 50D-PIX	4	$3 \times 3 \text{ mm}^2$	20 pF
HPK 80C-PIX	4	$3 \times 3 \text{ mm}^2$	12 pF
HPK 50D	1	$\varnothing = 1.0 \text{ mm}$	2.9 pF
CNM-W9HG11	4	$3 \times 3 \text{ mm}^2$	22 pF
CNM-W11LGA35	1	$1.3 \times 1.3 \text{ mm}^2$	3.9 pF

Table 1: Linear dimensions and capacitances of the sensors used in these studies.

140 The list of sensors studied in this article, as well as the temperature and the sensor  
 141 bias voltage used during their operation are listed in Tab. 2.

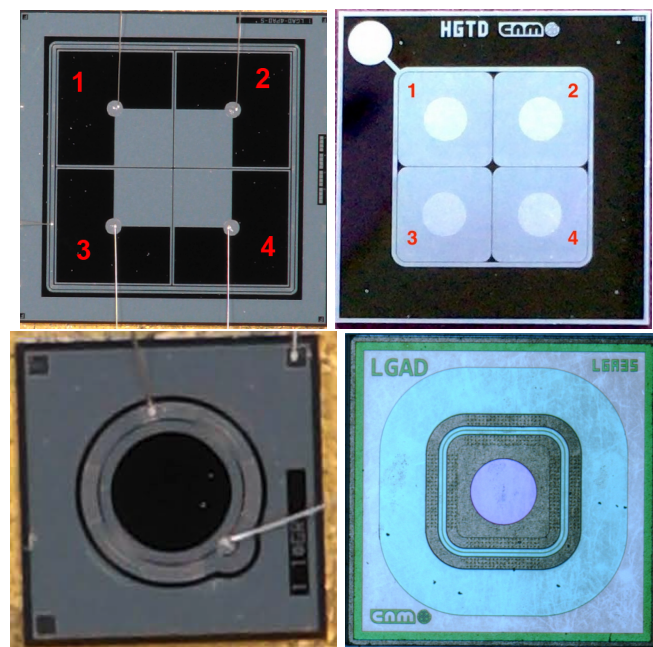


Figure 3: Photographs of the HPK 50D-PIX  $2 \times 2$  array sensor (top left), the CNM W9HG11  $2 \times 2$  array sensor (top right), the HPK 50D-GR single sensor (bottom left), and the CNM W11LGA35 single sensor (bottom right) are shown. Numerical labels overlaid on top of the images of the array sensors are used in the text when referring to individual pixels.

Sensor	KU Board 2-ch	UCSC board 4-ch	FNAL board 4-ch
HPK 50A-PIX	<b>-630 V (20)</b>	—	—
HPK 50B-PIX	<b>-550 V (25)</b>	—	—
HPK 50C-PIX	<b>-400 V (20)</b>	<b>-450 V (35)</b>	—
HPK 50D-PIX	<b>-300 V (30)</b>	—	<b>-250 V (17), -300 V (30), -250 V (29) -250 V (36)</b>
CNM W9HG11 $6 \times 10^{14} \text{ n/cm}^2$	—	<b>-180 V (14)</b>	—
CNM W11LGA35 $6 \times 10^{14} \text{ n/cm}^2$	—	<i>-600 V (20), -635 V (30)</i>	—
		<i>-400 V (24), -420 V (28)</i>	—

Table 2: Data taking conditions for the studies presented in this paper. Numbers in bold indicate that the sensor was at room temperature, underlined ones were taken at  $-10\text{C}^\circ$ , and those in italicized text were taken at  $-20\text{C}^\circ$ . The numbers in parenthesis indicate the gain at the given operation voltage.

#### 142 4. Readout Electronics

143 Three readout electronics boards were used in various measurements presented in this  
 144 paper. They were independently developed at Fermi National Accelerator Laboratory  
 145 (FNAL), at the University of Kansas (KU), and at the University of California Santa  
 146 Cruz (UCSC).

147 The 4-channel Fermilab LGAD test board is designed to test sensors up to 8.5 mm  
 148 by 8.5 mm at voltages up to 1 kV. Four wire-bonding pads allow for signal readout  
 149 via amplifiers based on Mini-Circuits GALI-66+. The amplifiers feature transformers  
 150 with 1:2 input impedance matching, two stages of amplification and a 500 MHz low-  
 151 pass filter. In this full configuration, the amplifiers feature  $12.5 \Omega$  input impedance,  $5 \text{ k}\Omega$   
 152 transimpedance, 500 MHz bandwidth and 1 mV rms output noise. If needed it is possible  
 153 to jump the input transformer and/or the low-pass filter, which would result in an input  
 154 impedance of  $50 \Omega$ , transimpedance of  $10 \text{ k}\Omega$ , and bandwidth of 2 GHz.

155 The 2-channel KU board, designed and produced by the University of Kansas, can  
 156 accommodate many types of sensors including diamond, silicon, LGAD or avalanche  
 157 photodiodes (APD). The sensor is hosted on the board itself and the electronics was  
 158 optimized for precise timing measurements. In particular, the amplifier, made with  
 159 discrete components, has an input impedance of  $700 \Omega$ , an output noise of 4 mV and a  
 160 gain in transresistance of about  $50 \text{ mV}/\mu\text{A}$  with a 3 dB bandwidth of 100 MHz. Those  
 161 values were simulated for an input capacitance of 20 pF, which corresponds roughly to  
 162 an LGAD of  $9 \text{ mm}^2$ . The power consumption of the board is about 130 mW per channel.

163 The UCSC 1-channel board is described in detail in Ref. [? ]. This board uses discrete  
 164 components and contains several features which allow for maintaining a wide bandwidth  
 165 ( $\sim 2 \text{ GHz}$ ) and a low noise even in noisy environments. The inverting amplifier uses a  
 166 high-speed SiGe transistor which has a transimpedance of about  $470 \Omega$ . A commercial  
 167 inverting amplifier with gain 10x is used to boost the signal. The 4-channel UCSC board  
 168 has two stages: the first one is identical to the UCSC single channel board, and is followed  
 169 by an inverting stage. The total transimpedance is  $10.7 \text{ k}\Omega$ .

#### 170 5. Timestamp Reconstruction

171 As discussed in Section 2, the reference time is measured using the Photek MCP-  
 172 PMT detector. The timestamp for this reference detector is obtained by fitting the peak

173 region of the pulse to a Gaussian function and the mean parameter of the Gaussian is  
 174 assigned as the timestamp  $t_0$ . A more detailed description can be found in Ref [? ].

175 The timestamp for signals from the LGAD sensors is obtained in two different ways  
 176 depending on which read-out board was used. For the FNAL and UCSC boards, whose  
 177 pulse widths are less than 2 ns, the timestamp is obtained via a fit to a Gaussian function  
 178 analogous to what is done for the reference detector. For the KU board, whose pulses  
 179 take much longer to fall to the baseline, the timestamp is obtained by performing a linear  
 180 fit to the rising edge of the pulse, between 15% and 70% of the maximum amplitude, and  
 181 the time at which the pulse reaches 45% of the maximum amplitude is assigned as its  
 182 timestamp  $t_1$ . We refer to this algorithm as the constant fraction discriminator (CFD)  
 183 method. This procedure is slightly different compared to previous studies of LGAD  
 184 sensors, where the CFD method was used uniformly.

185 The choices of the timestamp reconstruction algorithms listed above were motivated  
 186 by the result of a dedicated study of various algorithms for each of the three readout  
 187 boards. The study is performed using signals from the HPK 50D sensor. Constant  
 188 fraction discriminant (CFD) and constant threshold discriminant (CTD) algorithms are  
 189 used and the time resolution performance is studied as a function of the threshold used. In  
 190 Tables 3 and 4, we show the time resolution obtained for different thresholds for the CFD  
 191 and CTD algorithms respectively, for the KU readout board. For the CFD algorithm, we  
 192 observed no significant dependence of the timestamp on the pulse height of the signal.  
 193 However, for the CTD algorithm, the timestamp does depend on the pulse height and  
 194 requires a correction referred to as a time-walk correction. For most situations, the time-  
 195 walk correction can be accurately described by a linear dependence of timestamp on  
 196 pulse height, however we do observe that as the CTD threshold increases, the time-walk  
 197 correction becomes more quadratic. In Table 4, the time resolution is reported for both  
 198 linear and quadratic time-walk corrections. We observe that the best results are obtained  
 199 for a CFD threshold at 45%. However the CTD algorithm at a moderate threshold does  
 200 yield comparable time resolutions.

CFD Threshold	Time Resolution
15%	45 ps
30%	40 ps
45%	38 ps
60%	39 ps

Table 3: Time resolution measured for the HPK 50D-PIX sensor on the KU readout board using the constant fraction discriminant algorithm.

CTD Threshold	Time Resolution (Linear Time-walk Correction)	Time Resolution (Quadratic Time-walk Correction)
12 mV	52 ps	51 ps
18 mV	46 ps	45 ps
24 mV	43 ps	42 ps
37 mV	41 ps	40 ps
49 mV	43 ps	39 ps
61 mV	43 ps	39 ps
73 mV	45 ps	40 ps

Table 4: Time resolution measured for the HPK 50D-PIX sensor on the KU readout board using the constant threshold discriminant algorithm.

201 In Table 5, we show the analogous study performed for the FNAL and UCSC readout  
 202 boards. As signals on these readout boards have fast decay times, the Gaussian fit yields  
 203 the best performance. As for the KU readout board, the CFD and CTD algorithms again  
 204 give similar performance for the FNAL and UCSC readout boards.

Timestamp Algorithm Type	Time Resolution (FNAL Board with (HPK 50D-PIX Sensor)	Time Resolution (UCSC Board with irradiated HPK 50D Sensor)
Gaussian Fit	42 ps	35 ps
CFD at 15% Threshold	71 ps	47 ps
CFD at 30% Threshold	60 ps	42 ps
CFD at 45% Threshold	53 ps	39 ps
CFD at 60% Threshold	56 ps	44 ps
CTD at 18 mV Threshold (Linear Time-walk Correction)	55 ps	43 ps
CTD at 18 mV Threshold (Quadratic Timewalk Correction)	52 ps	37 ps

Table 5: Time resolution measured for the HPK 50D-PIX sensor on the FNAL readout board and the irradiated HPK 50D sensor on the UCSC board for a variety of timestamp reconstruction algorithms.

## 205 6. Sensor Studies and Analysis

206 We present a number of different studies performed on the LGAD sensors described  
 207 in Section 3. They include signal response uniformity, gap distance between adjacent  
 208 pixels, doping profile and sensor thickness characterization, temperature and irradiation  
 209 dependence, and time resolution. A brief overview of the analysis methods is given below,  
 210 followed by subsections describing the details and results of each study.

211 Events are required to have a signal in the Photek MCP-PMT consistent with a  
 212 minimum ionizing particle (MIP), and a signal above the noise in LGAD sensors. The  
 213 signal selection in the Photek MCP-PMT is the same for all runs and requires that the  
 214 signal is consistent with a MIP corresponding to amplitude values in the range between  
 215 160 mV and 320 mV. Signal events in LGAD sensors are selected such that they are  
 216 above the noise levels listed for each board in Sec. 4. All measurements other than those  
 217 described in Sec. 6.5 and 6.6 were performed at room temperature.

218 Here, and in the remainder of this article, whenever a scan of a certain characteristic  
 219 quantity – e.g. time resolution – of the sensor is presented, we show the X-axis scan for  
 220 pixels 1 and 2, and the Y-axis scan for pixels 1 and 3, as defined on the left picture in  
 221 Fig. 3. The X-axis scan across pixels 3 and 4, and Y-axis scan across pixels 2 and 4 show  
 222 qualitatively the same features, and are not presented here. Measurements presented  
 223 for various sensors were obtained from different datasets and therefore the statistical  
 224 precision is not always the same. The reason that in some measurements the error bars  
 225 are not the same across either X- or Y-coordinate is due to the fact that the beam does  
 226 not uniformly illuminate the whole sensor area, and hence the number of events is not  
 227 the same across sensor surface.

### 228 6.1. Study of the uniformity of the LGAD sensors

229 We present in detail uniformity studies – including signal detection efficiency, most  
 230 probable value, time difference, and time resolution – across the sensitive area of the

231 LGAD. The sensors under study were produced by HPK and CNM. The largest dataset  
 232 was collected for the HPK 50D-PIX and the CNM W9HG11 sensors. The HPK 50D-PIX  
 233 sensor was mounted on the 4-channel FNAL board and biased to  $-300$  V, while the CNM  
 234 W9HG11 sensor was mounted on the 4-channel UCSC board and biased to  $-180$  V. Both  
 235 sensors were operated at room temperature for these studies.

236 The measurements of the particle detection efficiency are shown in Fig. 4. Efficiency  
 237 is defined as the ratio of events that register a signal above the noise level to those that  
 238 contain a track identified by the pixel telescope pointing at the LGAD sensor. Error bars  
 239 in all efficiency measurements are evaluated as Clopper-Pearson intervals for calculating  
 240 binomial confidence intervals. Noise values for different boards used in the experiments  
 241 are listed in Sec. 4, and were measured using dedicated runs with no particles, and  
 242 data collected using random triggers. Signals used in the efficiency measurements were  
 243 required to have amplitude above 20 mV plots, well above the noise level.

244 We observe a flat 100% efficiency across the whole sensor area. The left edge in the  
 245 X-axis scan of pixel 1 on HPK 50D-PIX sensor in Fig. 4 is outside the acceptance of the  
 246 pixel telescope, hence the efficiency curve does not fully cover its surface. A clear drop  
 247 in efficiency is observed in the transition (“no-response”) region between the two pixels.  
 248 A more detailed study of the “no-response” region is given in Sec. 6.2.

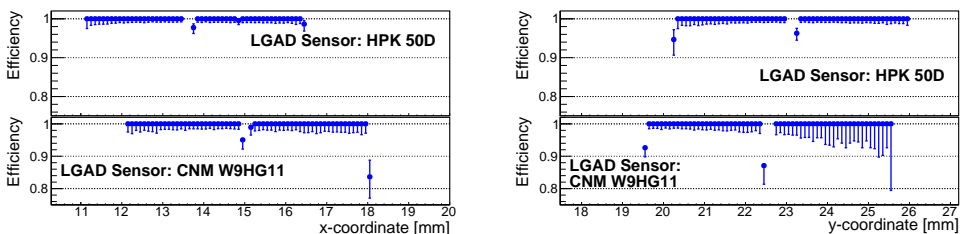


Figure 4: Efficiency measurement across the X-axis (left) and Y-axes (right) of the HPK 50D-PIX sensor mounted on the FNAL board, and the CNM W9HG11 sensor mounted on the UCSC board. The scans of pixels 1 and 2 along the X-axis, and pixels 1 and 3 along the Y-axis are shown. The pixel numbering scheme is defined in Fig. 3.

249 An important characteristic is the uniformity of the signal size across the surface of the  
 250 sensor, which directly impacts on its timing performance. We use the signal amplitude  
 251 as the metric to characterize the signal size uniformity. The distribution of the LGAD  
 252 signal amplitudes is fitted to a Landau distribution. An example of the fit is shown in  
 253 Fig. 5. The most probable value (MPV) parameter of the fitted Landau distribution is  
 254 plotted in Fig. 6. A flat response with a uniform signal size is observed over the whole  
 255 sensor area. As a study of systematic effects, we have also repeated the fit using the  
 256 convolution of a Landau function and a Gaussian function to model the impact of noise  
 257 and fluctuations in the multiplication process. We find that the peak location increases  
 258 systematically by about 5% for all points in a correlated fashion. However it does not  
 259 appear to impact the conclusions drawn on the response uniformity.

260 The measurements of the time difference  $\Delta t = t_1 - t_0$  between the reference timestamp  
 261 ( $t_0$ ) and the timestamp of the LGAD sensors ( $t_1$ ) are shown in Fig. 7. The micro-bonding  
 262 scheme of the HPK and CNM  $2 \times 2$  sensor arrays is shown in Fig. 3. For the HPK sensor,  
 263 the  $\Delta t$  dependence on the hit position indicates a shift of about 20–30 ps between the

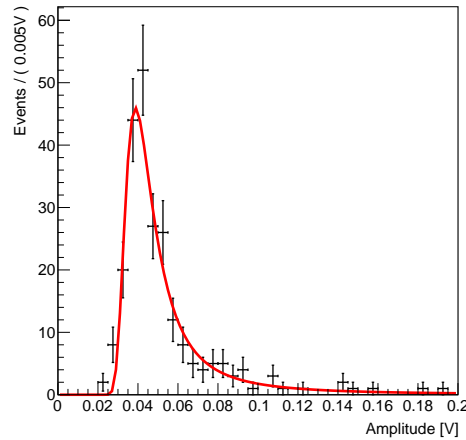


Figure 5: The signal amplitude distribution is fitted to a Landau function. The data corresponds to one bin of the X-axis scan.

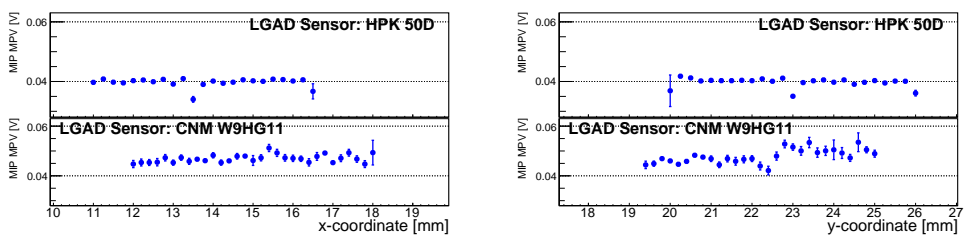


Figure 6: Signal amplitude MPV measurement across the X-axis (left) and Y-axes (right) of the HPK 50D-PIX sensor mounted on the FNAL board, and the CNM W9HG11 sensor mounted on the UCSC board. The scans of pixels 1 and 2 along the X-axis and pixels 1 and 3 along the Y-axis are shown. The pixel numbering scheme is defined in Fig. 3.

264 metalized area near the center of the array (gray region of the top-left image in Fig. 3)  
 265 and the non-metalized area. This effect cannot be attributed to the algorithm used to  
 266 time-stamp the events, since the same behavior is observed with the CFD and CDT  
 267 algorithms. Furthermore, the same behavior is observed on all HPK sensor varieties  
 268 mounted on KU board, as presented in Sec. 6.3. The CNM W9HG11 sensor does not  
 269 contain metalized areas on its surface and we do not observe the same effect. Further  
 270 studies are needed to understand the effect.

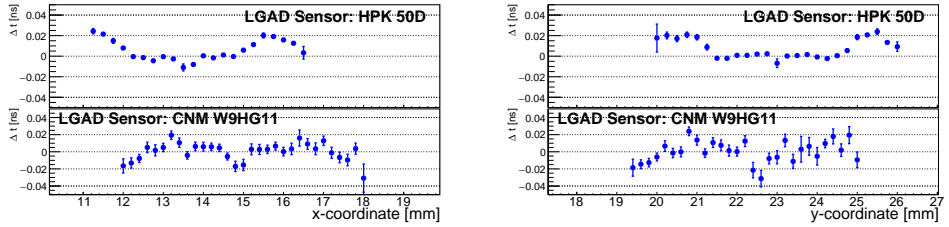


Figure 7:  $\Delta t$  measurement across the X- and Y-axes of the HPK 50D-PIX sensor mounted on the FNAL board, and the CNM W9HG11 sensor mounted on the UCSC board. The scans of pixels 1 and 2 along the X-axis, and pixels 1 and 3 along the Y-axis are shown. The pixel numbering scheme is defined in Fig. 3.

271 The measurement of the time resolution across the sensor surface is shown in Fig. 8.  
 272 The distribution of  $\Delta t$  between the timestamp of the LGAD signal and the reference  
 273 signal is fitted with a Gaussian function, and the spread  $\sigma$  of the fitted function is  
 274 defined as the time resolution. We observe a uniform time resolution around 40 ps across  
 275 the whole surface area for HPK, and around 55 ps for CNM sensors.

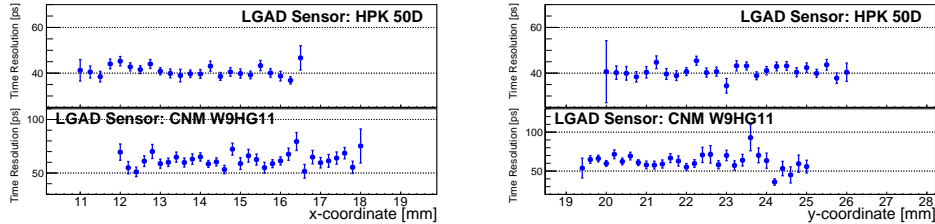


Figure 8: Time resolution measurement across the X-axis (left) and Y-axes (right) of the HPK 50D-PIX sensor mounted on the FNAL board, and the CNM W9HG11 sensor mounted on the UCSC board. The scans of pixels 1 and 2 along the X-axis, and pixels 1 and 3 along the Y-axis are shown. The pixel numbering scheme is defined in Fig. 3.

### 276 6.2. Measurement of the “no-response” area between two neighboring pixels

277 In order to precisely measure the width of the no-response area between two neigh-  
 278 boring pixels, a large statistics sample of about 350,000 events was collected with the  
 279 HPK 50D-PIX sensor mounted on a 2-channel KU board. The sensor was biased to  
 280  $-300$  V. The large dataset allowed us to perform a detailed scan in the area between  
 281 the two pixels as shown in Fig. 9. In order to estimate the width of the no-response  
 282 between the pixels, the efficiency curves of the two neighboring pixels are fitted with an

283 S-curve function of the form  $y = p_1 \times \text{Erf}\{\pm(p_2 - x)/p_3\} + p_4$ , where  $\text{Erf}\{x\}$  is the error  
 284 function defined as:

$$\text{Erf}(x) = \frac{2}{\sqrt{\pi}} \times \int_0^x e^{-t^2} dt \quad (1)$$

285 , and  $p_i$  were free parameters of the fit. We define the width of the “no-response” area as  
 286 the distance between the 90% efficiencies on the two fitted S-curves, as shown in Fig. 9.  
 287 We measure the width of the no-response area on the HPK 50D-PIX sensor to be 170  $\mu\text{m}$ ,  
 288 with an uncertainty of 15  $\mu\text{m}$ . Data points outside the sensor area in Figs. 9, 10 actually  
 289 had hit the sensor active area, but the coordinate of the track is incorrectly assigned,  
 290 due to a small probability (< 1%) to misreconstruct the position of the track.

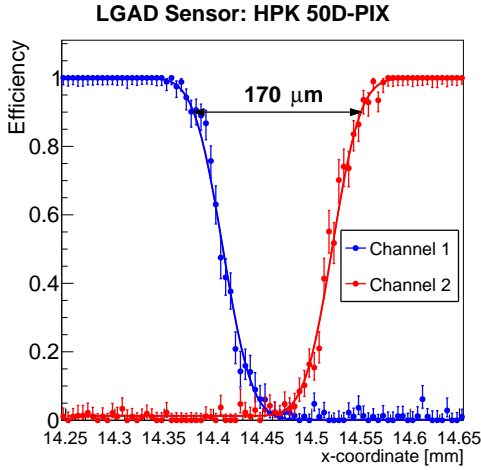


Figure 9: A zoom-in version of the efficiency measurement as a function of the X position of the beam particle. The HPK 50D-PIX sensor was operated at  $-300$  V bias voltage. The pixel numbering scheme is defined in Fig. 3.

291 A further measurement was made on the 4-channel UCSC board for the HPK 50C-  
 292 PIX sensor and the CNM W9HG11 sensor. We compare the width of the gap region of  
 293 the HPK and CNM sensors in Fig. 10. Both sensors in this comparison were tested in  
 294 the beam simultaneously. The HPK 50C-PIX sensor was operated at  $-450$  V, and CNM  
 295 W9HG11 sensor was operated at  $-180$  V. We measure the size of the “no-response”  
 296 region to be around 150  $\mu\text{m}$  on the HPK 50C-PIX – compatible with the HPK 50D-  
 297 PIX sensor – and around 130  $\mu\text{m}$  for the CNM sensor. Both measurements have an  
 298 uncertainty of 15  $\mu\text{m}$ .

### 299 6.3. Comparison of HPK doping profiles

300 Studies of the dependence of the sensors’ characteristics on the doping concentra-  
 301 tions were performed by comparing the 50  $\mu\text{m}$  HPK PIX sensors of different gain splits.  
 302 In order to reduce the impact of the variations between different readout boards, all  
 303 measurements presented in this section were performed using only 2-channel KU readout  
 304 boards. Four readout boards were prepared, each with an HPK sensor mounted on it, and

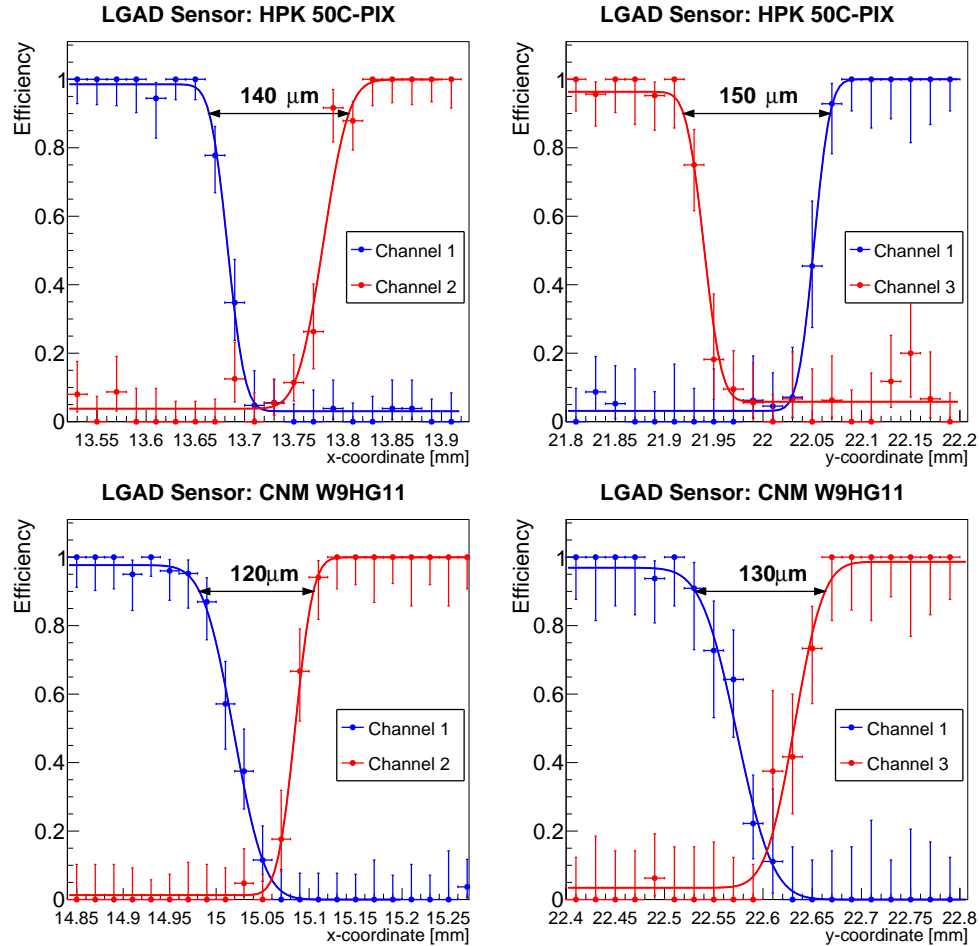


Figure 10: A zoom-in version of the efficiency measurement across the X- and Y-axes of the HPK 50C-PIX (top) and CNM W9HG11 (bottom) sensors. HPK sensor is operated at  $-450$  V, and CNM sensor is operated at  $-180$  V. Data points in blue are those from one pixel, and data points in red are from the neighboring pixel. The blue and red curves are fitted to the data points as described in the text. Arrows indicate the distance between the half-maximum points of the fitted curves.

305 tested in the beam. Data taken with the HPK 50D-PIX is the same as that presented  
306 in Fig. 9, which is the largest data sample collected during this test beam campaign.  
307 Therefore, the statistical uncertainties in the measurements of the HPK 50A-, B-, and  
308 C-PIX sensors are larger than those of 50D-PIX. For this study, the sensors were oper-  
309 ated at room temperature, and their bias voltages were set to  $-630$  V,  $-550$  V,  $-400$  V,  
310 and  $-300$  V for the HPK 50A-PIX, HPK 50B-PIX, HPK 50C-PIX, and HPK 50D-PIX  
311 sensors, respectively.

312 The distribution of the MPV of signal amplitudes across the sensor area is shown  
313 in Fig. 11, where the MPV is extracted as described in Sec. 6.1. Comparing the signal  
314 amplitudes between the two pixels we observe that the average amplitude varies between  
315 the two channels. However, in Fig. 6 we observed that the amplitudes in the two pixels  
316 of the same HPK 50D-PIX sensor on the FNAL readout board do not show the same  
317 variations. We conclude that the observed difference in amplitude is due to imperfec-  
318 tions in the manufacturing process of the custom-designed pre-amplifiers used in the KU  
319 readout board and not due to sensor properties. Nevertheless, the signal MPV within a  
320 single pixel is highly uniform for all tested samples.

321 The measurements of the time difference between the reference timestamp and the  
322 timestamps of the HPK sensors are shown in Fig. 12. As was shown in Fig. 7, the  $\Delta t$   
323 exhibits an offset of about 20 ps between the metalized area and the non-metalized area  
324 of the sensor. The feature is present in all 4 types of the HPK PIX sensors, does not  
325 depend on the readout board or timestamp reconstruction algorithm used, and appears  
326 to be statistically consistent in shape and magnitude.

327 The measurements of the time resolution across the sensors are shown in Fig. 13. We  
328 observe a uniform time resolution around 40 ps across the entire sensor area.

#### 329 6.4. Comparison of uniformity of HPK $50\ \mu\text{m}$ with $80\ \mu\text{m}$

330 The thickness of the active area of the sensor is an important design parameter when  
331 optimizing for time resolution. A detailed study of time resolution of HPK sensors of  $80$   
332 and  $50\ \mu\text{m}$  is presented in [? ]. Here we compare the uniformity of the time resolution  
333 across the sensors of these two thicknesses. This study is performed using the HPK  
334 C-PIX sensors with the same dopant concentration. The  $80\ \mu\text{m}$  sensor HPK 80C-PIX  
335 is biased at  $-610$  V, while the  $50\ \mu\text{m}$  sensor HPK 50C-PIX is biased at  $-400$  V. The  
336 sensor's gains at these bias voltages are: about 11 for the  $80\ \mu\text{m}$  sensor, and about 20  
337 for the  $50\ \mu\text{m}$  sensor. The time resolution for the two sensors are shown in Fig. 14 as  
338 a function of position, and exhibit fairly uniform behavior. Measurements of the HPK  
339 50C-PIX sensor were performed on the KU 2-channel board, and those for HPK 80C-PIX  
340 used the FNAL 4-channel board.

#### 341 6.5. Temperature dependence of the LGAD sensors

342 In order to maintain their optimal performance at the highest fluences envisioned at  
343 the HL-LHC, the LGAD sensors will be cooled to temperatures below  $-20^\circ\text{C}$  degrees.  
344 Operation at such low temperatures will allow to significantly reduce the leakage current.  
345 The sensors yield higher gain at lower temperatures, but at the cost of a lower breakdown  
346 voltage. Therefore, it is important to study the impact of the temperature on the gain and  
347 time resolution, as well as their uniformity. In this section we describe the measurements  
348 of the LGAD sensors performed at  $-10$  and  $-20^\circ\text{C}$  degrees, and compare the results to

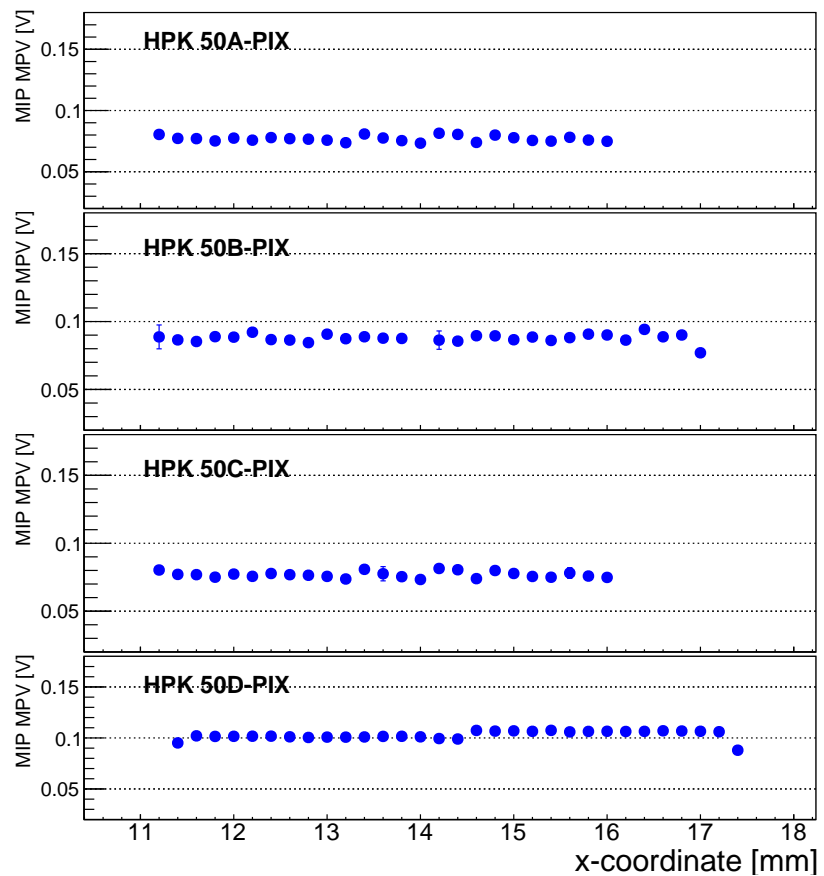


Figure 11: Signal amplitude MPV measurement across the X-axis of the HPK 50A-, 50B-, 50C-, and 50D-PIX sensors mounted on the KU board. The scan of pixels 1 and 2 along the X-axis, and pixel numbering scheme is defined in Fig. 3.

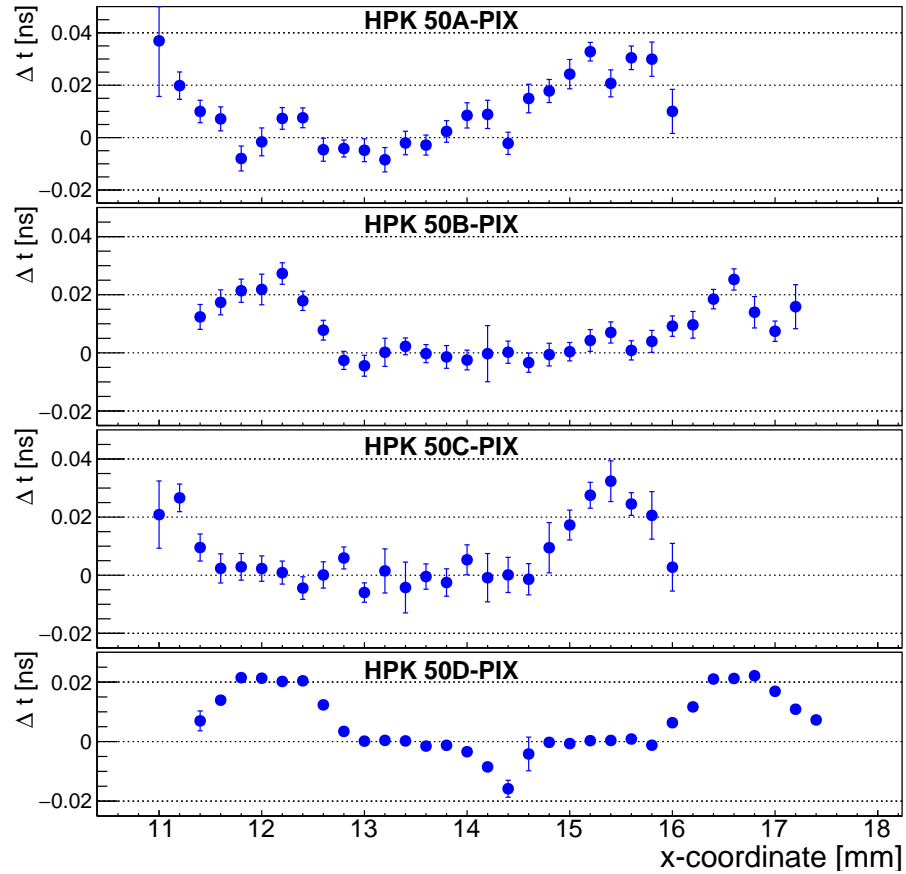


Figure 12:  $\Delta t$  measurements as a function of the X position of the beam particle for the HPK 50A-, 50B-, 50C-, and 50D-PIX sensors mounted on the KU board. The scan of pixels 1 and 2 along the X-axis is shown. The pixel numbering scheme is defined in Fig. 3.

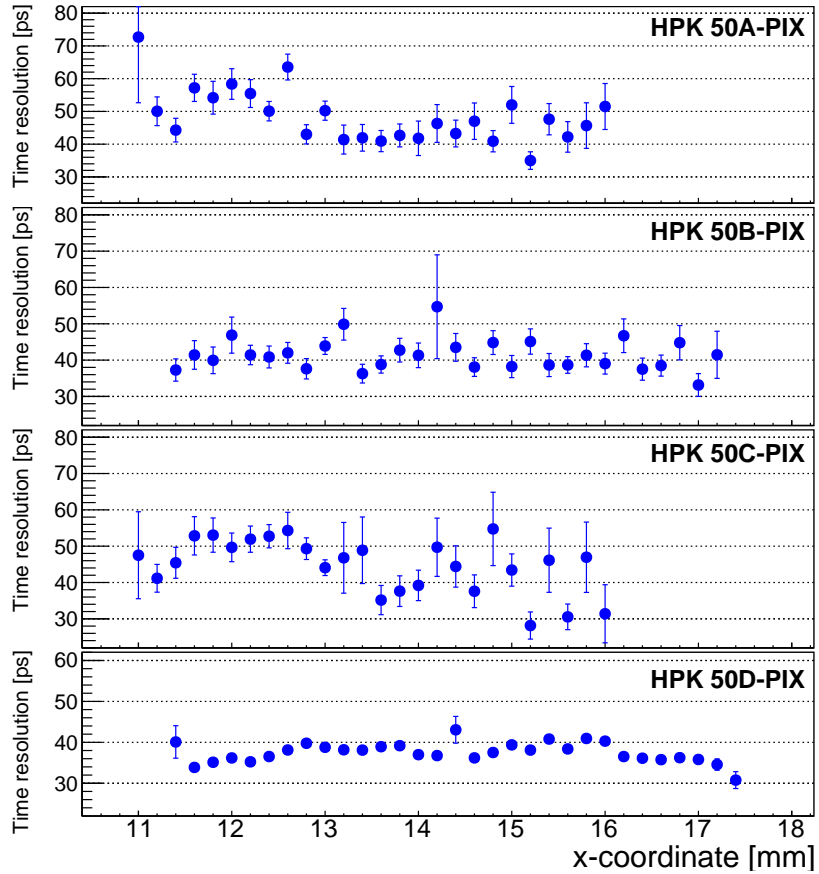


Figure 13: Time resolution measurements as a function of the X position of the beam particle for the HPK 50A-, 50B-, 50C-, and 50D-PIX sensors mounted on the KU board. The scan of pixels 1 and 2 along the X-axis is shown. The pixel numbering scheme is defined in Fig. 3.

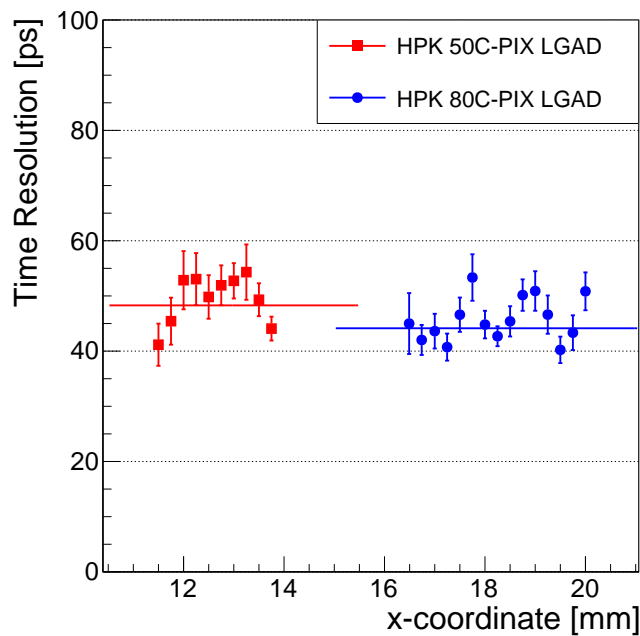


Figure 14: Comparison of the uniformity of the measured time resolution of the HPK 80C-PIX versus 50C-PIX sensors. The  $80 \mu\text{m}$  sensor is mounted on the FNAL board, and is biased at -610 V, and the  $50 \mu\text{m}$  sensor is mounted on the KU board and is biased at -400 V. The lines show fits of the data to constant functions.

349 those at room temperature. These measurements were performed with the HPK 50D-  
 350 PIX sensors mounted on the FNAL 4-channel board. The sensor was biased at the same  
 351 voltage of  $-250$  V for all temperature scenarios. The HPK 50D gain at this bias voltage  
 352 and at  $+20^{\circ}\text{C}$  was measured to be around 17, while at  $-20^{\circ}\text{C}$  and the same bias voltage  
 353 it was measured to be around 36.

354 The distribution of the signal MPV across the sensor surface is shown in Fig. 15. We  
 355 observe that the signal MPV increases by more than a factor of two when the temperature  
 356 is reduced from  $+20^{\circ}\text{C}$  to  $-20^{\circ}\text{C}$ . While the MPV uniformity across the two channels  
 357 are within 2% of each other at room temperature, at lower temperatures one of the pixels  
 358 shows a difference of about 5% with respect to its neighboring pixel. A more detailed  
 359 study is needed to understand whether this difference is due to non-uniform temperature  
 360 distribution across the sensor array or due to differences in the signal response between  
 361 different pixel sensors at colder temperatures.

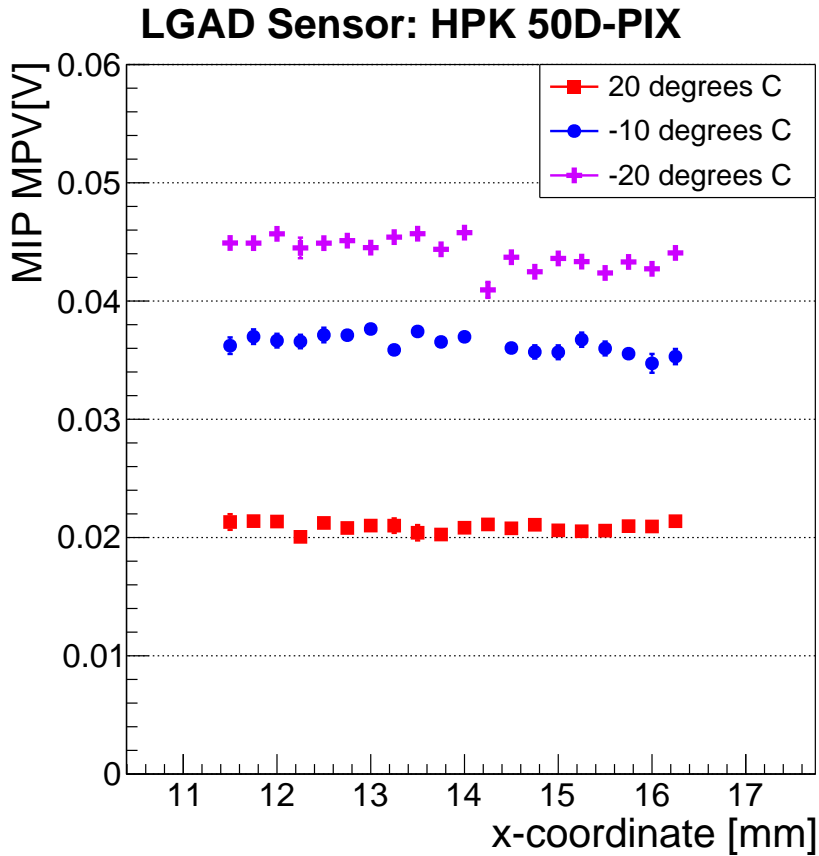


Figure 15: Temperature dependence of the signal amplitude MPV uniformity across the X-axis of the HPK 50D-PIX sensors mounted on the FNAL board. The scan of pixels 1 and 2 along the X-axis is shown, and pixel numbering scheme is defined in Fig. 3. The HPK sensor is biased at  $-250$  V.

362 The distribution of the  $\Delta t$  between the reference timestamp and the timestamp from  
 20

363 the HPK 50D-PIX sensor is shown in Fig. 16. We observe no significant changes in the  
364 behavior of the  $\Delta t$  as the temperature varies.

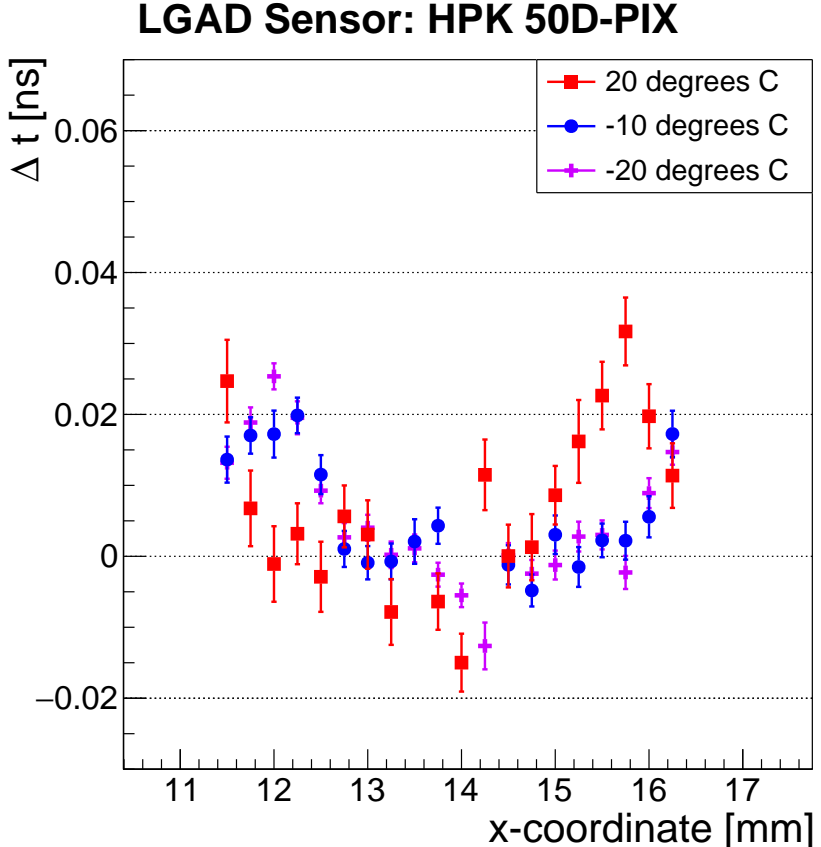


Figure 16: Temperature dependance of the  $\Delta t$  uniformity across the X-axis of the HPK 50D-PIX sensors mounted on the FNAL board. The scan of pixels 1 and 2 along the X-axis is shown, and pixel numbering scheme is defined in Fig. 3. The HPK sensor is biased at  $-250$  V.

365 The time resolution measured for the HPK 50D-PIX sensor is shown in Fig. 17. We  
366 observe a significant improvement in the time resolution as the temperature is lowered  
367 from  $+20^{\circ}\text{C}$  to  $-20^{\circ}\text{C}$  degrees. As the temperature is lowered, the signal-to-noise ratio  
368 improves as the gain of the LGAD sensor increases. Generally, the electronic noise may  
369 also decrease as the temperature is lowered, but in our case it was observed to remain  
370 relatively constant at  $1.2$  mV for both  $+20$  and  $-20^{\circ}\text{C}$ . Therefore the improvement comes  
371 mainly from the increase in the signal gain. The time resolution was measured to improve  
372 from around  $55\text{-}60$  ps at the room temperature, down to  $35\text{-}40$  ps at  $-20^{\circ}\text{C}$ . It is worth  
373 noting that time resolution around  $35$  ps with pixels of area  $9\text{ mm}^2$  is a promising result  
374 for cost-effective implementation in LHC experiments.

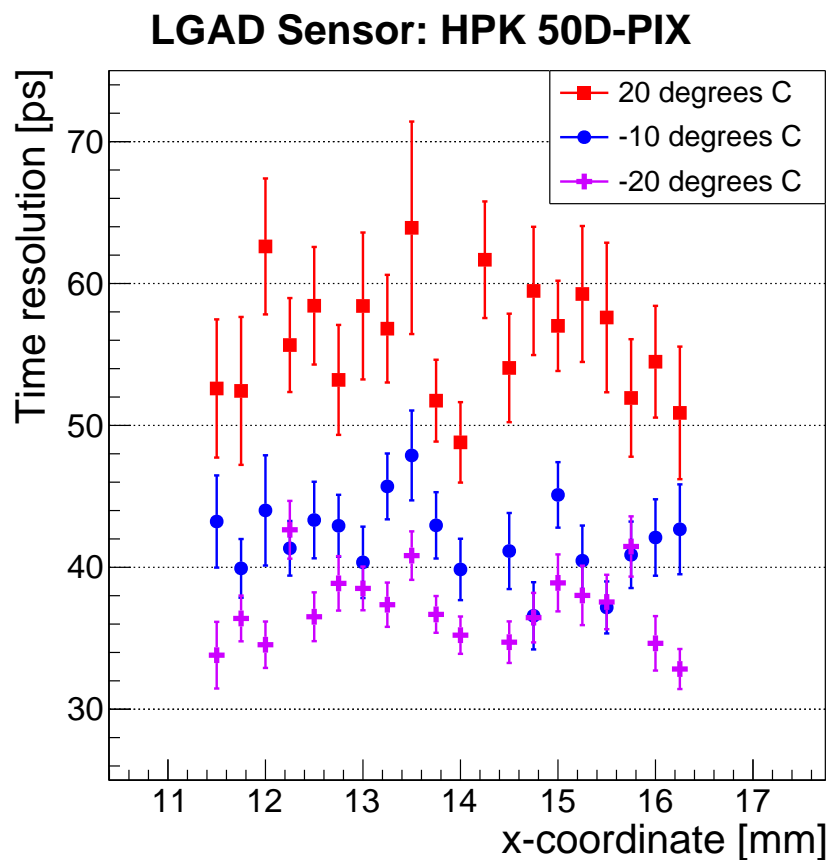


Figure 17: Temperature dependance of the time resolution uniformity across the X-axis of the HPK 50D-PIX sensors mounted on the FNAL board. The scan of pixels 1 and 2 along the X-axis is shown. The pixel numbering scheme is defined in Fig. 3. The HPK sensor is biased at  $-250$  V.

375    6.6. Radiation tolerance of the LGADs

376    In this section we present the studies of the irradiated HPK and CNM sensors, which  
 377    were exposed to neutron irradiation at the Ljubljana TRIGA reactor [? ]. The neutron  
 378    spectrum and flux are well known and the fluence is quoted in 1 MeV equivalent neutrons  
 379    per cm<sup>2</sup> ( $n_{eq.}/cm^2$  or n/cm<sup>2</sup> for short). After  $6 \times 10^{14}$  n/cm<sup>2</sup> irradiation, the devices were  
 380    annealed for 80 min at 60°C. Afterward the devices were kept at -20°C degree during  
 381    storage, transportation, and test beam experiments. Effects of neutron irradiation on  
 382    LGAD sensors is documented in [? ], [? ], and [? ].

383    The two-dimensional distribution of the signal amplitudes on the surface of the ir-  
 384    radiated sensors are shown in Figs. 18 and 19. From the comparison with the image  
 385    of the CNM sensor shown in Fig. 3 and the distribution in Fig. 18, it is clear that two  
 386    distinct regions can be identified on the sensor based on the signal amplitude: the region  
 387    under the aluminum metalization on the periphery of the sensor, and the region without  
 388    aluminum metalization in the center. The distribution on the right of Fig. 18 shows that  
 389    at the same bias voltage the amplitude under the aluminum (periphery) is about 2.5  
 390    times larger than that without aluminum (center). The amplitude scan of the irradiated  
 391    HPK 50D sensor is shown on the left panel of Fig. 19, and a uniform amplitude across  
 392    the sensor surface is observed, which can also be seen on the right panel of Fig. 19. In  
 393    contrast to the CNM sensor, the whole surface of the active area of the HPK 50D sensor  
 394    is without metalization

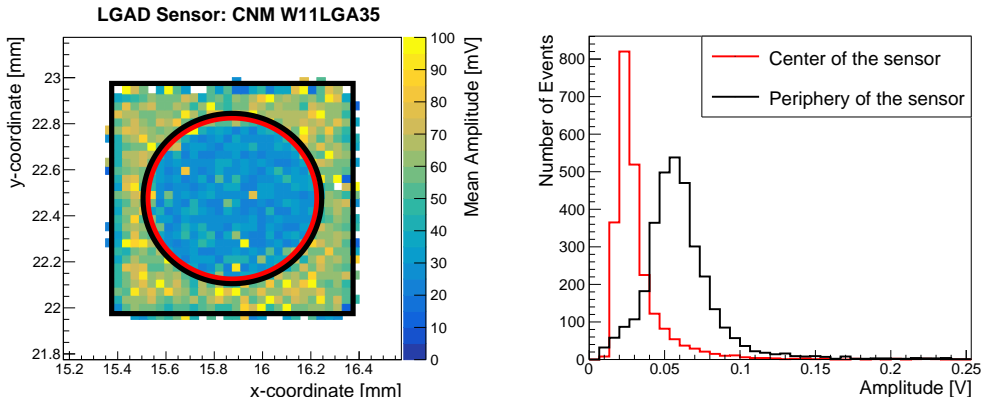


Figure 18: (Left) The map of the amplitude distribution on the irradiated CNM W11LGA35 sensor across X and Y coordinates. Two distinct regions on the sensor surface can be identified according to the amplitude distribution: the center of the sensor (area within the red circle), and the periphery of the sensor (area between the black circle and black square). (Right) Amplitude distribution in the two areas of the irradiated CNM W11LGA35 sensor. The sensor was irradiated to  $6 \times 10^{14}$  n/cm<sup>2</sup>. Measurements were performed at -20°C.

395    Measurements of the particle detection efficiency are shown in Fig. 20. These mea-  
 396    surements were performed with the HPK sensor biased at -600 V, and the CNM sensor  
 397    biased at -400 V. We observe a flat 100% efficiency across the whole HPK sensor area,  
 398    and the efficiency of the CNM sensor is also very close to 100%. As with the pixelated  
 399    array sensors, a clear drop in efficiency is observed near the edges of the active area.

400    The distribution of MPV of signal amplitudes across the sensor area is shown in

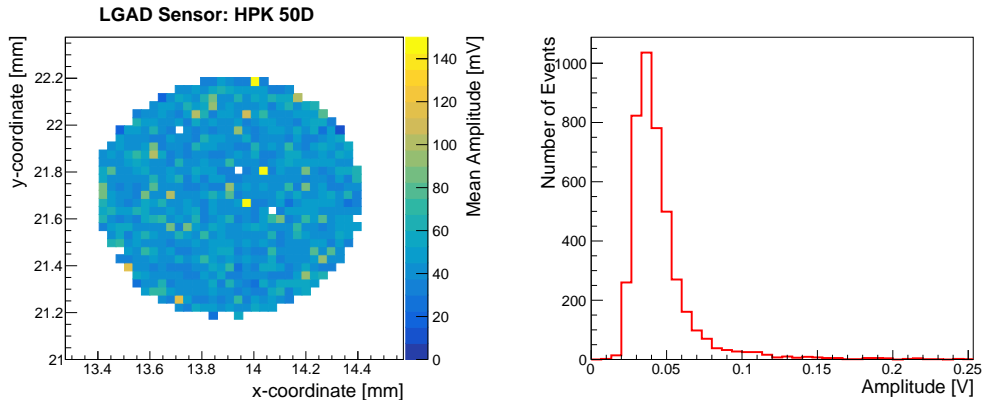


Figure 19: (Left) The map of the amplitude distribution on the irradiated HPK 50D sensor across X and Y coordinates. (Right) Signal amplitude distribution for the irradiated HPK 50D sensor. The sensor was irradiated to  $6 \times 10^{14}$  n/cm<sup>2</sup>. Measurements were performed at -20°C.

401 Fig. 21, where the MPV is extracted as described in Sec. 6.1. Measurements were per-  
 402 formed at two bias voltage values for both sensors: -600 and -635 V for HPK (gain  
 403 equal to 20 and 30, respectively), and -400 and -420 V for CNM sensors (gain equal to  
 404 24 and 28, respectively). A uniform signal amplitude is observed across the HPK sensor,  
 405 while for the CNM sensor the amplitude varies across the sensor surface, as observed also  
 406 in Fig. 18.

407 The distribution of the  $\Delta t$  between the reference timestamp and the timestamps of the  
 408 signals from the irradiated HPK and CNM sensors are shown in Fig. 22. Measurements  
 409 at both bias voltage values are presented. We measured a uniform distribution of the  
 410  $\Delta t$  values across the HPK sensor. The CNM sensor exhibits a non-uniformity across the  
 411 sensor surface, where the signals from the central, non-metallized area arrive about 10 ps  
 412 earlier than those from the peripheral, metallized area.

413 Distributions of the time resolution across the surface of the irradiated sensors are  
 414 shown in Fig. 23. The time resolution measured with the HPK sensor improves slightly  
 415 with the increase of the bias voltage, and shows a uniform distribution across the sensor  
 416 surface. In contrast, the CNM sensor shows a non-uniform distribution of time resolution,  
 417 which is a consequence of the variations of the signal amplitude across the sensor. We  
 418 observe that while the signal amplitudes increase a bit, the RMS of the noise also increases  
 419 from about 5.5 mV to 10 mV. As a consequence, we observe a small degradation of the  
 420 time resolution for the CNM sensor as the bias voltage is increased.

## 421 7. Conclusion

422 In a beam test at FNAL with tracking information, we compared the performance  
 423 of LGAD produced by CNM Barcelona and HPK Hamamatsu. Single pads of diameter  
 424 1 mm and  $2 \times 2$  arrays of square pixels of 3 mm were used. Sensors with thicknesses of  
 425 about 50 and 80  $\mu\text{m}$  were studied. The uniformity of the sensor response in pulse height,  
 426 efficiency, and timing resolution were studied. Four different readout boards were used  
 427 in these studies. The uniformity of the sensor response in pulse height before irradiation

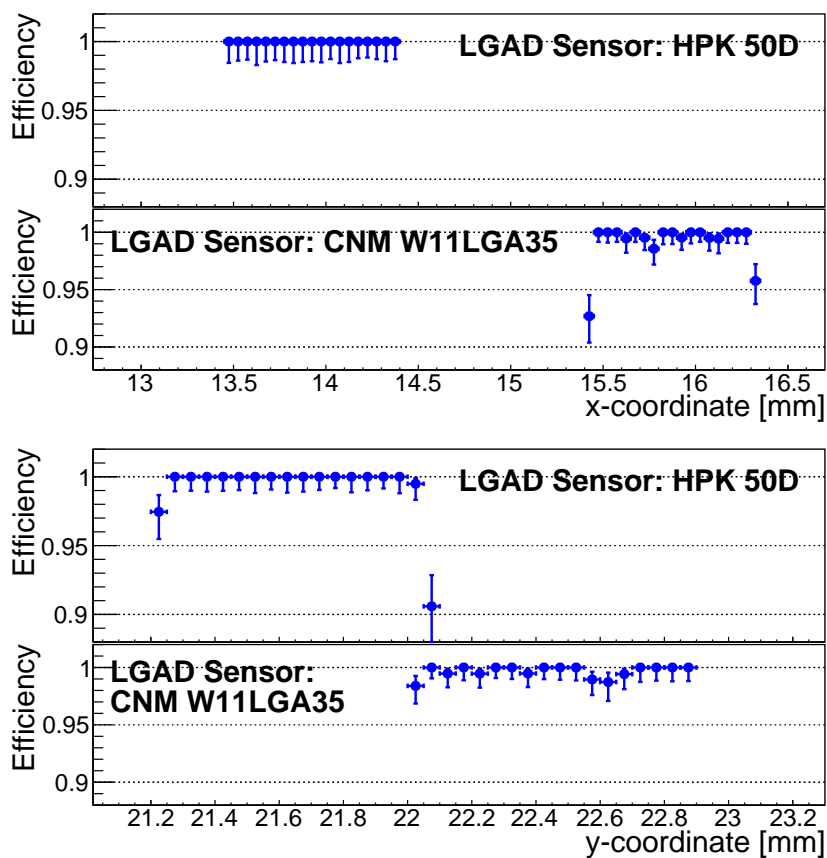


Figure 20: Efficiency measurements across the X-axis (top) and Y-axes (bottom) of the HPK 50D and CNM W11LGA35 irradiated sensors. Both sensors were irradiated to  $6 \times 10^{14} \text{ n/cm}^2$ . Measurements were performed at  $-20^\circ\text{C}$ .

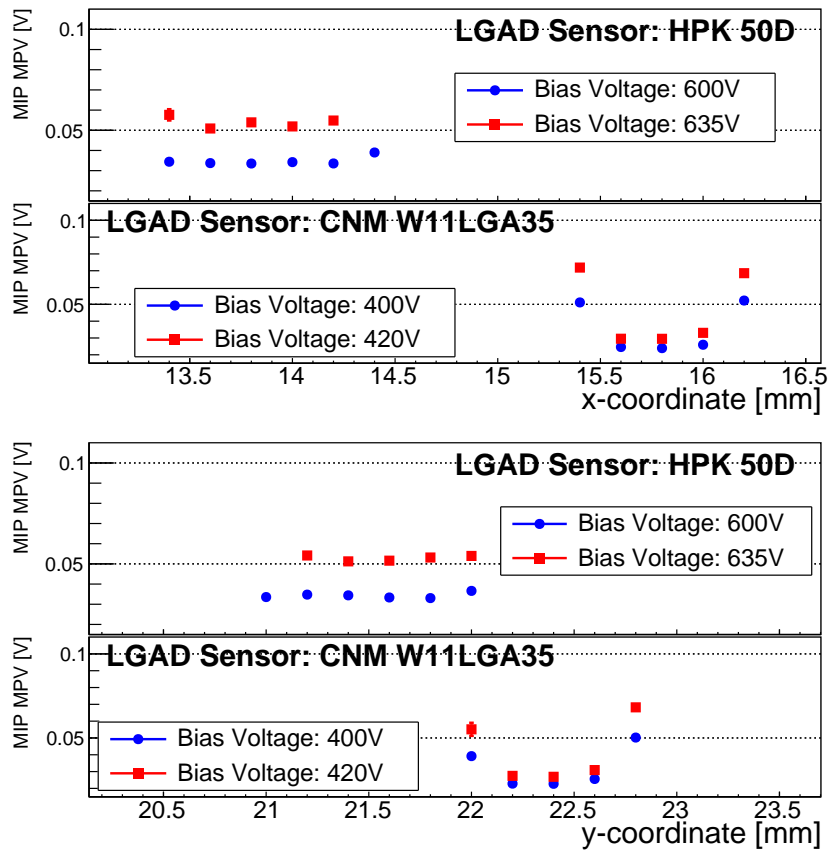


Figure 21: Signal amplitude MPV measurement across the X-axis (top) and Y-axes (bottom) of the HPK 50D and CNM W11LGA35 irradiated sensors. Both sensors were irradiated to  $6 \times 10^{14} \text{ n/cm}^2$ . Measurements were performed at  $-20^\circ\text{C}$ .

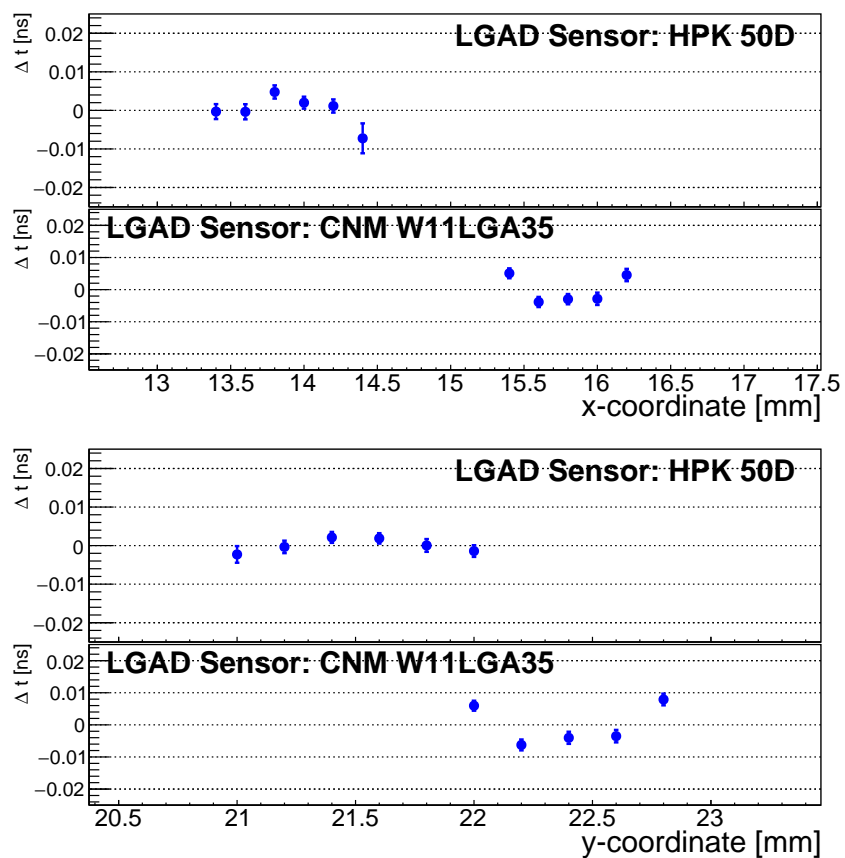


Figure 22:  $\Delta t$  measurements across the X-axis (top) and Y-axes (bottom) of the HPK 50D and CNM W11LGA35 irradiated sensors. Both sensors were irradiated to  $6 \times 10^{14}$  n/cm<sup>2</sup>. Measurements were performed at  $-20^{\circ}\text{C}$ .

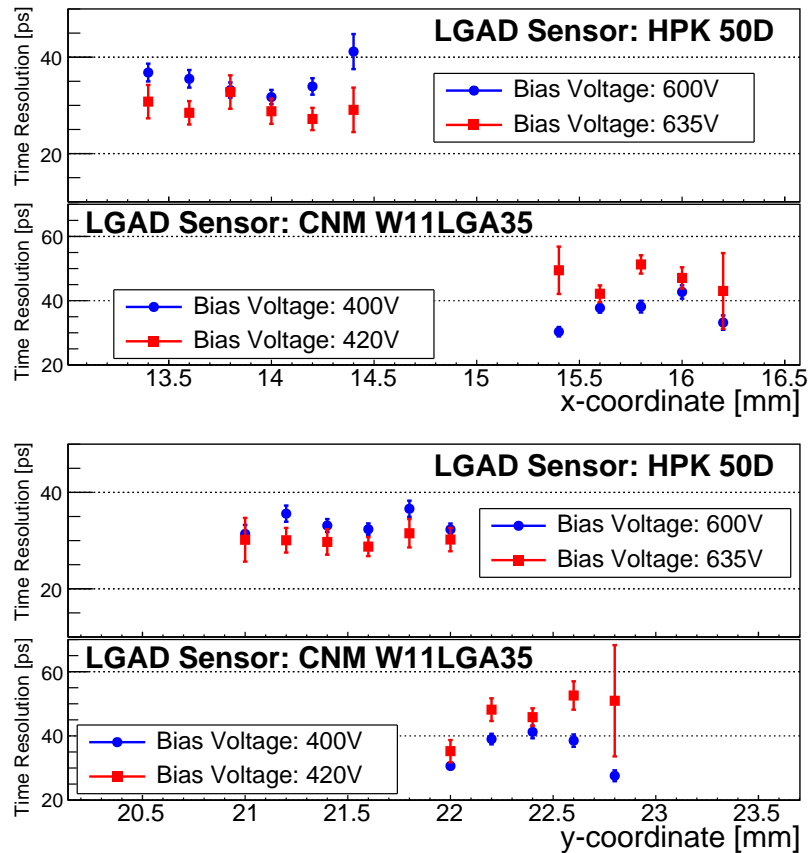


Figure 23: Time resolution measurements across the X-axis (top) and Y-axes (bottom) of the HPK 50D and CNM W11LGA35 irradiated sensors. Both sensors were irradiated to  $6 \times 10^{14} \text{ n/cm}^2$ . Measurements were performed at  $-20^\circ\text{C}$ .

428 was found to have a 2% spread. The efficiency and timing resolution before irradiation  
429 were found to be 100% and 30-40 ps, respectively. The “non-response” region between  
430 pixels was measured to be about  $130\text{ }\mu\text{m}$  for CNM sensors and  $170\text{ }\mu\text{m}$  for HPK sensors.  
431 A small timing shift across the HPK sensor of the order 20–30 ps can be explained by  
432 the observed change in pulse shape when comparing metalized and non-metalized sensor  
433 areas. Uniform signal detection efficiency of 100% is observed on all sensors, both before  
434 and after irradiation.

435 For an un-irradiated  $50\text{ }\mu\text{m}$  thick LGADs with 3 mm pads we find the following timing  
436 results:

- 437 • at a temperature of  $+20^\circ\text{C}$ , the timing resolution ranges from 40 ps to 50 ps  
438 depending on the readout board.
- 439 • cooling the LGAD, while keeping the bias voltage the same at  $-250\text{ V}$ , improves  
440 the timing resolution from 55 ps at  $+20^\circ\text{C}$  to 43 ps at  $-10^\circ\text{C}$  to 36 ps at  $-20^\circ\text{C}$ .

441 After a neutron fluence of  $6 \times 10^{14}\text{ n/cm}^2$ , the single pad CNM sensor exhibits a  
442 large gain variation of a factor 2.5 when comparing metalized and non-metalized sensor  
443 areas. For an  $50\text{ }\mu\text{m}$  thick LGAD with 1 mm pads irradiated  $6 \times 10^{14}\text{ n/cm}^2$  we find the  
444 following timing results when operated at  $-20^\circ\text{C}$ :

- 445 • for the HPK LGAD the highest bias voltage reached is  $-635\text{ V}$  and the correspond-  
446 ing timing resolution is 30 ps;
- 447 • for the CNM LGAD the highest bias voltage reached is  $-420\text{ V}$  and the correspond-  
448 ing timing resolution is 30 ps for the metalized area and 40 ps for the non-metalized  
449 area.

## 450 Acknowledgment

451 Dedicated to the memory of our friend, brilliant researcher, and wonderful colleague  
452 Anatoly Ronzhin.

453 We thank the FTBF personnel and Fermilab accelerator’s team for very good beam  
454 conditions during our test beam time. We also appreciate the technical support of the  
455 Fermilab SiDet department for the rapid production of wire-bonded and packaged LGAD  
456 assemblies. We would like to thank Alan Prosser and Ryan Rivera for their critical help  
457 in setting up the DAQ and trigger chain. We thank Ned Spencer, Max Wilder, and Forest  
458 McKinney-Martinez for their technical assistance, and the CNM and HPK manufacturing  
459 team. We acknowledge the help of V. Cindro and I. Mandic with the neutron irradiations.

460 This document was prepared using the resources of the Fermi National Accelerator  
461 Laboratory (Fermilab), a U.S. Department of Energy, Office of Science, HEP User Facil-  
462 ity. Fermilab is managed by Fermi Research Alliance, LLC (FRA), acting under Contract  
463 No. DE-AC02-07CH11359. Part of this work was performed within the framework of  
464 the CERN RD50 collaboration.

465 This work was supported by the Fermilab LDRD 2017.027; by the United States  
466 Department of Energy grant DE-FG02-04ER41286; by the California Institute of Tech-  
467 nology High Energy Physics under Contract DE-SC0011925; by the European Union’s  
468 Horizon 2020 Research and Innovation funding program, under Grant Agreement no.

<sup>469</sup> 654168 (AIDA-2020) and Grant Agreement no. 669529 (ERC UFSD669529); by the  
<sup>470</sup> Italian Ministero degli Affari Esteri and INFN Gruppo V; and by the Spanish Min-  
<sup>471</sup> istry of Economy, Industry and Competitiveness through the Particle Physics National  
<sup>472</sup> Program (ref. FPA2014-55295-C3-2-R and FPA2015-69260-C3-3-R) co-financed with  
<sup>473</sup> FEDER funds.

<sup>474</sup> **References**